ORIGINAL PAPER

CrossMark

Facile synthesis of $ZnMn_2O_4$ nanosheets via cathodic electrodeposition: characterization and supercapacitor behavior studies

Houshang Barkhordari[1] · Hamid Heydari[2] · Azad Nosrati[3] · Jamil Mohammadi[4]

Abstract

In this work, we report a facile chemical precipitation method to prepare zinc manganite ($ZnMn_2O_4$) materials. $ZnMn_2O_4$ nanosheets were synthesized through a cathodic electrolytic electrodeposition (ELD), and their application as supercapacitor electrodes were evaluated. The effect of calcining temperature on the nanostructure and morphology of $ZnMn_2O_4$ was investigated systematically through scanning electron microscopy (SEM), energy-dispersive X-ray spectroscopy (EDS), FTIR spectroscopy, X-ray diffractometery (XRD), X-ray photoelectron spectroscopy (XPS), and Brunauer-Emmett-Teller (BET) surface area measurements. Electrochemical properties of the synthesized products as electrodes in a supercapacitor device were studied using cyclic voltammetry (CV), galvanostatic charge/discharge, and electrochemical impedance spectroscopy in aqueous electrolyte. $ZnMn_2O_4$ nanosheets exhibiting remarkable electrochemical performance in supercapacitors with specific capacitance ($\sim$457 F g^{-1} at 1 A g^{-1}), excellent rate capability (67.2% capacity retention at 10 A g^{-1}), and good cycling stability (only 92.5% loss after 4000 cycles at 3 A g^{-1}). All the results demonstrate that the synthesis route is cost-effective, facile, and can development for prepared electrode materials in electrochemical supercapacitors.

Keywords Cathodic electrolytic electrodeposition (ELD) · Crystallinity · $ZnMn_2O_4$ nanosheets · Supercapacitor

Introduction

With the destroy energy, reducing available of energy sources and increasing environmental pollution, the importance of energy conversion and storage has gone up. In the recent years, supercapacitors (electrochemical capacitors) are considered as one of the most important energy storage devices, and as powerful tools for future energy conversion and storage. They have received high attention, likely due to their prominent advantages such as high power densities, fast charge/recharge capability, long cycle life, and adequate safety [1–4]. However,

supercapacitors have defects such as low energy density, high cost, and relatively low rate capability, which limit their practical applications. Thus, solving these problems is one of development fields of supercapacitors [5, 6].

Energy storage mechanism in supercapacitors can be performed in two different ways: the double-layer formation at electrode/electrolyte interface that will be in electric double-layer capacitor (EDLC) and redox reactions in electrode involving faradic processes that will be in pseudocapacitor faradaic supercapacitors (FS) [7]. Amount of charge storage in EDLCs is mainly limited on available active surface area (that is why low specific capacitances have in this regard). For example, activated carbons are known to have very high specific surface area (up to $\sim$2500 m^2 g^{-1}) but low specific capacitances (up to $\sim$280 F g^{-1}) [8]. Because of strong dependence of FS mechanism on the redox reactions (surface area has less important), they usually show higher capacitances and energy density in comparison with EDLCs. However, a FS usually suffers from relatively lower power density compared with EDLSs. It can be as results of faradaic processes that are normally slower than non-faradaic processes.

Materials undergoing such redox reactions include conducting polymers and several metal oxides. In general,

✉ Jamil Mohammadi
jamilmohammadi.1990@gmail.com

1 Faculty of Mechanical and Energy Engineering, Shahid Beheshti University, P.O. Box 16589-53571, Tehranpars, Tehran, Iran

2 Faculty of Sciences, Razi University Kermanshah, P.O. Box 671496-7346, Kermanshah, Iran

3 Faculty of Sciences, University of Tehran, P.O. Box 14155-6455, Enghelab Avenue, Tehran, Iran

4 Faculty of Chemistry, Shahid Beheshti University, G. C., 1983963113, Evin, Tehran, Iran

metal oxides because of higher energy density than conventional carbon materials and better electrochemical stability than polymer materials have been effectively employed as the electrode materials for advanced supercapacitors [9]. In recent years, metal oxides such as MnO_2 [10, 11], NiO [12, 13], Co_3O_4 [14, 15], and CuO [16, 17] have been efficiently employed as electrodes for supercapacitors. Other characteristics such as low cost, toxicity, controllable structure, and unique morphology in electrode materials should be considered [18]. Nowadays, a group of transition-metal oxides with spinel structures (AB_2O_4) such as $NiCo_2O_4$ [19, 20], $MgCo_2O_4$ [21], $CuCo_2O_4$ [22], $ZnCo_2O_4$ [23–25], and $NiFe_2O_4$ [26] have been used as electrode materials for supercapacitors and Li-ion batteries (LIBs). This material exhibits excellent cycle stability and higher capacitance than single-component oxides due to their stronger electrochemical activities and richer redox reactions [27–32].

Following the ongoing research trends, another ternary spinel studied as electrode material for supercapacitors is zinc manganite ($ZnMn_2O_4$). $ZnMn_2O_4$ has been many applications in the Li-ion batteries, electrocatalysts, and magnetic materials [33–35]. Various synthetic methodologies to synthesize nanosized $ZnMn_2O_4$ have been reported in previous researches [36–39]. Nanofibers and nanowebs $ZnMn_2O_4$ synthesized by electrospinning technique [36] and nanocrystalline produced by the polymer pyrolysis method [40] have shown a capacity retention of 705, 530, and 569 mA h g^{-1} in Li-ion battery electrodes after prolonged cycling, respectively.

In the recent years, there has been published some reports for application of $ZnMn_2O_4$ in supercapacitor electrode materials. Spherical morphology of $ZnMn_2O_4$ synthesized by urea combustion method exhibits specific capacitance of 160 F g^{-1}, energy density of 18 W h kg^{-1}, and power density of 185 W kg^{-1} [41]. The obtained porous $ZnMn_2O_4$ microspheres on different substrates including Ti sheet, carbon cloth, and nickel foam by hydrothermal technique have shown specific capacitance of 127, 50, and 155 F g^{-1}, respectively [42].

Specific capacitance and cycle stability are two main factors of supercapacitor electrode materials which will be employed for improving $ZnMn_2O_4$. In this paper, for the first time, we reported the synthesis of $ZnMn_2O_4$ nanosheets via cathodic electrolytic electrodeposition (ELD) method. ELD can fulfill the drawbacks of the previous reports because of being such a facile, low cost, and less time-consuming method with almost identical morphology. This method involves ELD to grow Zn–Mn hydroxide precursor on the surface of stainless steel, and in the next step, calcining temperature treatment is used to convert the Zn–Mn hydroxide precursor into $ZnMn_2O_4$. The effect of calcining temperature on the $ZnMn_2O_4$ supercapacitor device performance was also tested. The $ZnMn_2O_4$ nanosheets are found to show a high specific capacitance of ~457 F g^{-1} at a current density of 1 A g^{-1} and long-term cycling stability (92.5% of its original value after 4000 cycles). Finally, the electrochemical parameters obtained in the present work were compared to the previous reported methods.

Experiment

Analytical grade chemicals $Zn(NO_3)_2.6H_2O$ and $Mn(NO_3)_2.4H_2O$ were purchased from Merck (Darmstadt, Germany). Deionized water was obtained through a Millipore water purification system (Milford, MA, USA). The graphite anodes were purchased from local suppliers, and research-grade stainless steel (SS; grade 316 L, 0.2 mm thick) sheets were used for preparation of electrode.

Synthesis of $ZnMn_2O_4$

$ZnMn_2O_4$ spinel was synthesized by a two-step process. In the first step (Fig. 1), galvanostatic deposition of Zn–Mn hydroxide was on both sides of the stainless steel cathode by using aqueous mixed electrolyte of $Zn(NO_3)_2.6H_2O$ and $Mn(NO_3)_2.4H_2O$ (0.005:0.01 in molar ratio). Two parallel planar graphite elec-

Fig. 1 Schematic representation of the preparation of $ZnMn_2O_4$
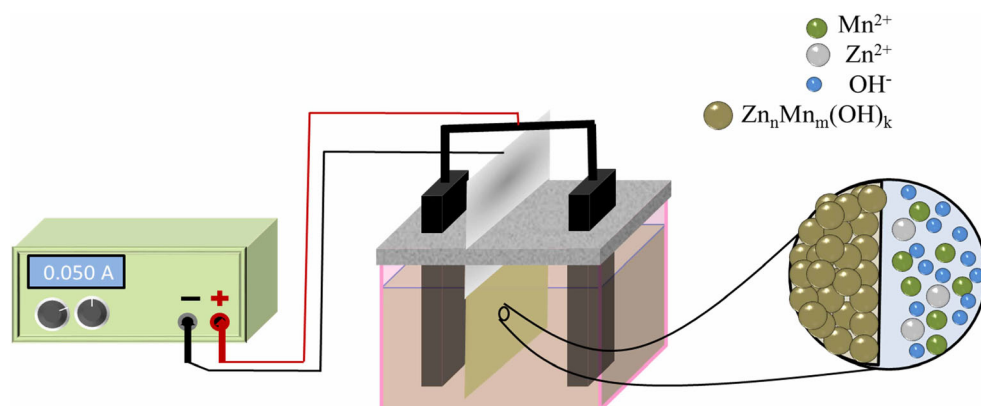
trodes of the same dimensions were placed in the solution working as counteranodes. Electrodeposition reactions was carried out at a constant current density of 0.5 mA cm^{-2}. After electrodeposition, the deposited film was washed immediately with deionized water and dried at room temperature for 3 h. In the next step, thermal calcining of the deposit on stainless steel was done at 250, 450, and 650 °C for 2 h.

Physical and electrochemical characterization

The surface morphology and chemical composition of the synthesized samples were examined by means of a TESCAN MIRA3 FEG scanning electron microscope (SEM) equipped with an energy-dispersive X-ray spectroscopy (EDS) detector. The crystalline structures of the synthesized samples were characterized by Cu-κα line (λ = 1.5406 nm) from a STOEXD-3A X-ray diffractometer (XRD). FTIR spectra of powder samples in KBr pellet form were recorded on BOMEM MB-series FTIR spectrometer within the wave number in range of 250 to 4000 cm^{-1}. X-ray photoelectron spectroscopy (XPS; X-Ray 8025-Bestec, Germany) was used to investigate the surface chemical composition of the products. The data were acquired using a monochromic Al-Kα X-ray source (hν = 1486.6 eV) operating at a vacuum better than 10^{-7} Pa. The nitrogen adsorption-desorption isotherms were obtained at 77 K using micrometritics ASAP 2020 sorptometer. Specific surface area was determined with Brunauer-Emmett-Teller (BET) equation, and the distribution of pore size was calculated from the adsorption curve by the Barrett-Joyner-Halenda (BJH) method. Electrochemical tests were performed using a Autolab PGSTAT100 potentiostat/galvanostat. The following equation is used to calculate the specific capacitance:
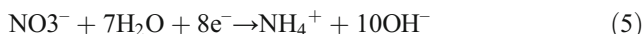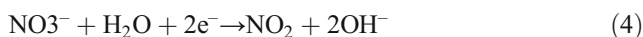
$$C_s = \frac{I\Delta t}{m\Delta\nu} \tag{1}$$

where C_s is the specific capacitance, I is the applied current (mA), Δt is the discharging time (s), m is the mass of the electrode (g), and $\Delta\nu$ is the discharging potential range (V).

Results and discussion

Morphology and structural analysis

The mechanism of synthesis of metal oxides/hydroxides by cathodic electrodeposition has been discussed in the previous report [43]. Local pH increased at the cathode surface because of various cathodic reactions including the reduction of water, dissolved oxygen, and nitrate ions that lead to OH$^-$ ions as described in the following reactions [44, 45]:

$$2H_2O + 2e^- \rightarrow H_2 + 2OH^- \tag{2}$$

$$O_2 + 2H_2O + 4e^- \rightarrow 4OH^- \tag{3}$$

$$NO_3^- + H_2O + 2e^- \rightarrow NO_2 + 2OH^- \tag{4}$$

$$NO_3^- + 7H_2O + 8e^- \rightarrow NH_4^+ + 10OH^- \tag{5}$$

With producing the OH$^-$ ions at the surface cathode electrode, uniform precipitation of mixed metal hydroxides ($Zn_m(OH)_n$, $Mn_p(OH)_q$) are formed on the surface of cathode electrodes. Considering the values of solubility product constant (Ksp) at 25 °C for Zn(OH)$_2$ (3×10^{-16}) and Mn(OH)$_2$ (2.5×10^{-13}), the following equation can be proposed (Eq. (6)):

$$nZn^{2+} + mMn^{2+} + kOH^- \rightarrow Zn_nMn_m(OH)_k \tag{6}$$
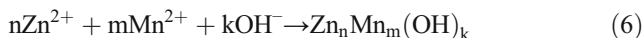
The followed calcination process involved an oxidation reaction that convert the $Zn_nMn_m(OH)_k$ precursor into spinel $ZnMn_2(O)_4$ (Eq. (7)):

$$Zn_nMn_m(OH)_k + \frac{1}{2}O_2 \rightarrow ZnMn_2(O_4) + k/2H_2O \tag{7}$$
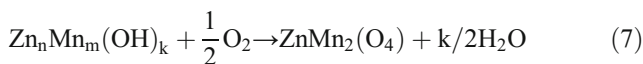
In order to identify crystallographic structure of the ZnMn$_2$O$_4$ nanostructures calcined, the powder XRD was studied. Figure 2 shows the XRD patterns of the calcined samples at different temperatures (250–650 °C), where the diffraction peaks at 2θ values of 18.22°, 29.32°, 33.00°, 36.41°, 59.01°, and 60.82° are ascribed to the reflection of (1 0 1), (1 1 2), (1 0 3), (2 1 1), (3 2 1), and (2 2 4) planes of the tetragonal spinel ZnMn$_2$O$_4$, respectively. These

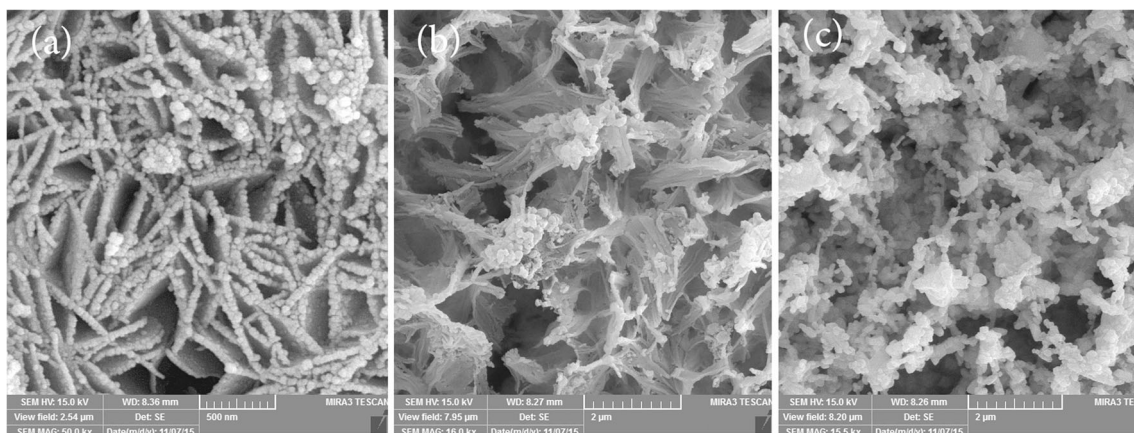Fig. 2 XRD patterns collected for ZnMn$_2$O$_4$ at 250, 450, and 650 °C over 10° to 80° 2θ range
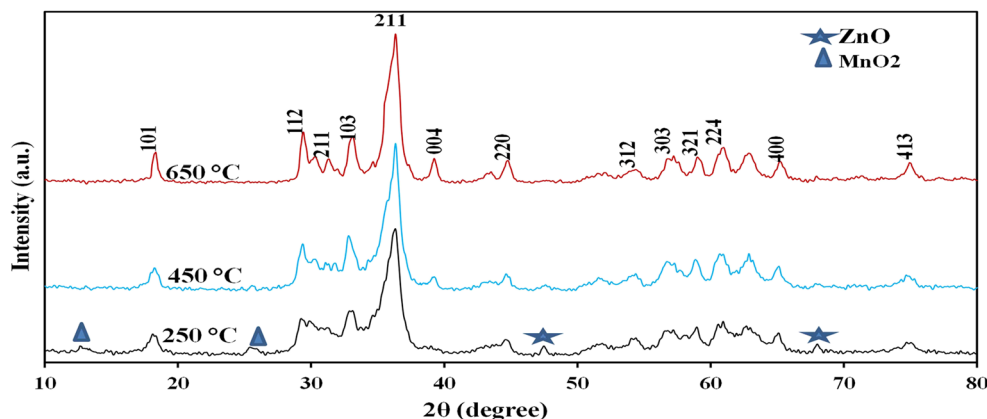
Fig. 3 SEM images for as-synthesized ZnMn$_2$O$_4$ nanostructure after calcining at **a** 250 °C, **b** 450 °C, and **c** 650 °C

observations are in good agreement with the standard data given by JCPDS 01-077-0470. In the products which were calcined at 250 °C, the peaks related to MnO$_2$ and ZnO could still be observed. However, for the samples treated at 450 and 650 °C, intensity of these peaks reduced and precursors were converted into spinel ZnMn$_2$O$_4$. With increasing the calcination temperature from 250 to 650 °C, relative intensities of the characteristic peaks for ZnMn$_2$O$_4$ nanostructures are increased and the peaks width gradually narrow. For this reason, the percent crystallinity of spinel ZnMn$_2$O$_4$ was growing and transforming from the disordered to a more ordered structure [46].

The optimized calcining temperature of ZnMn$_2$O$_4$ was evaluated through morphology characterization by scanning electron microscopy. Figure 3 shows the SEM images of the ZnMn$_2$O$_4$ obtained at the different temperature including 250, 450, and 650 °C. At 250 °C, a network of ZnMn$_2$O$_4$ nanosheets spread over the entire surface was obtained (Fig. 3a). The thickness of the nanosheets were in the range regions of 20–60 nm. It is noteworthy that the network-like structure (which consists of interconnected nanosheet) shows anisotropic morphology characteristics and the formation of a loosely packed microstructures in the nanometer scale. As shown in Fig. 3b, the morphology of ZnMn$_2$O$_4$ obtained at calcined temperature of 450 °C have nano-flake structure (the

thickness of the nanoflakes 55–150 nm). However, some submicroparticles in the SEM images at 450 °C are visible. As the temperature is increased to 650 °C, obtained ZnMn$_2$O$_4$ is composed of submicron-sized agglomerate particles which might be due to the expansion crystallization of ZnMn$_2$O$_4$ (Fig. 3c). The main reason for changing the morphology with increasing the calcination temperature to 650 °C is recrystallization and agglomeration of the primary particles [47, 48]. These images show that optimization of calcining temperature in ELD method is critical for obtaining a better morphology.

To understand the presence of some functional groups on the calcined ZnMn$_2$O$_4$, we conducted FT-IR spectrum analysis. The IR spectra of the prepared samples treated at 250, 450, and 650 °C are presented in Fig. 4a. One can assign the band at 3420 cm^{-1} to O–H stretching vibration and two bands at 1630 and 1040 cm^{-1} to O–H bending vibrations associated with Mn atoms [49]. As can be seen from the figure, the intensities of these bands are very low in heat-calcined sample, indicating the water escape from the sample during the heat treatment. The spectrum of the precursor calcined at 250 °C shows that two bands at 498 and 617 cm^{-1} can be assigned to spinel ZnMn$_2$O$_4$. The bands belonging to ZnMn$_2$O$_4$ are considerably weak, probably because of the

Fig. 4 **a** FTIR spectra of as-prepared and heat calcined samples. **b** EDS spectrum of the ZnMn$_2$O$_4$ nanostructure at 250 °C
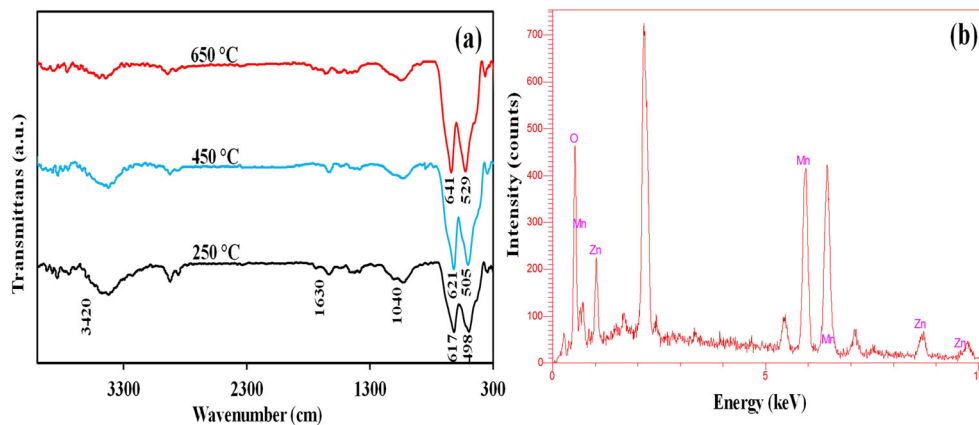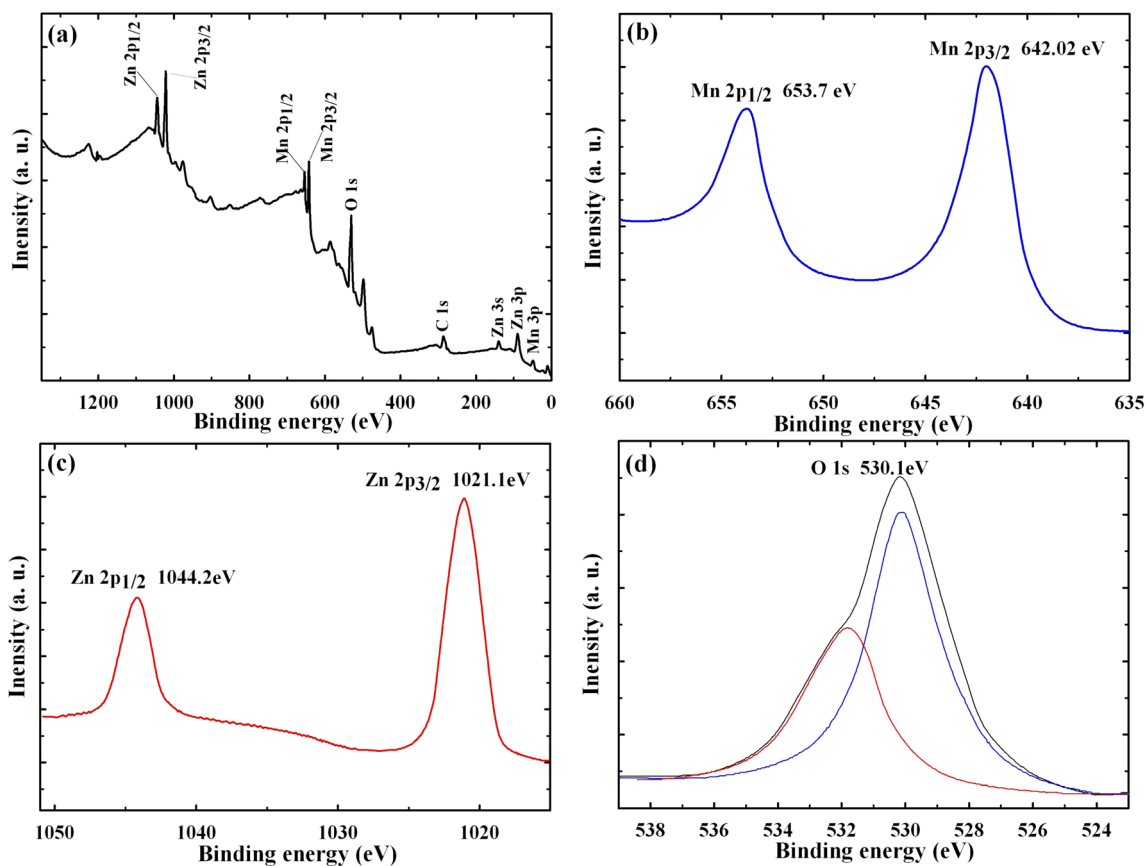
Fig. 5 The XPS spectrum of the $ZnMn_2O_4$ at 250: **a** survey spectrum and high-resolution **b** Mn 2p, **c** Zn 2p, and **d** O 1s

co-existence of MnO_2 and ZnO. When the temperature reached 650 °C, two strong bands at 529 and 641 cm^{-1} related to spinel $ZnMn_2O_4$ appear. These bands become more intense and shift to higher wave numbers, from 498 to 529 and from 617 to 641 cm^{-1}, which reveals that the formed spinel have achieved an improved crystallinity [50].

The chemical composition of the $ZnMn_2O_4$ nanosheets is investigated by EDS analysis (Fig. 4b). The results showed that the product contains only three types of elements including Zn, Mn, and O and atomic ratio of Zn:Mn:O is approximately 1:2:4. These results further confirm the formation of $ZnMn_2O_4$ pure phase.
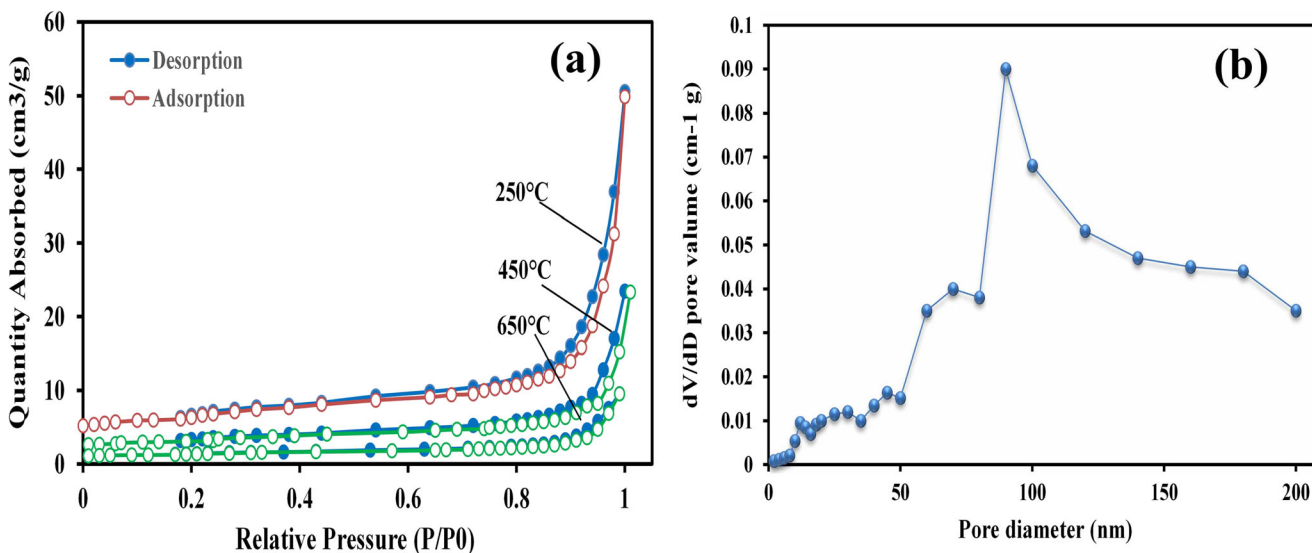

Fig. 6 **a** N_2 adsorption-desorption isotherms and **b** corresponding pore size distribution of the as-prepared $ZnMn_2O_4$ nanostructure obtained at 250 °C
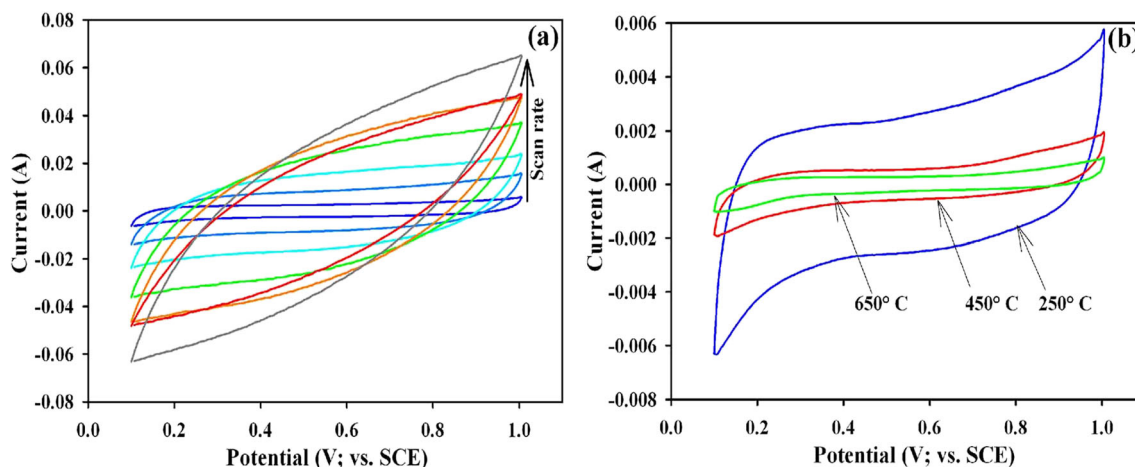
Fig. 7 **a** CV curves for ZnMn₂O₄ nanosheet electrodes measured at different scan rates of 1, 5, 10, 20, 30, 40, and 50 m V s⁻¹ in 0.5 M Na₂SO₄ in a three-electrode configuration with Pt electrode as the counterelectrode and SCE as the reference electrode. **b** CV curves for ZnMn₂O₄ at 250, 450, and 650 °C measured at 1 mV s⁻¹ in 0.5 M Na₂SO₄ in a three-electrode configuration
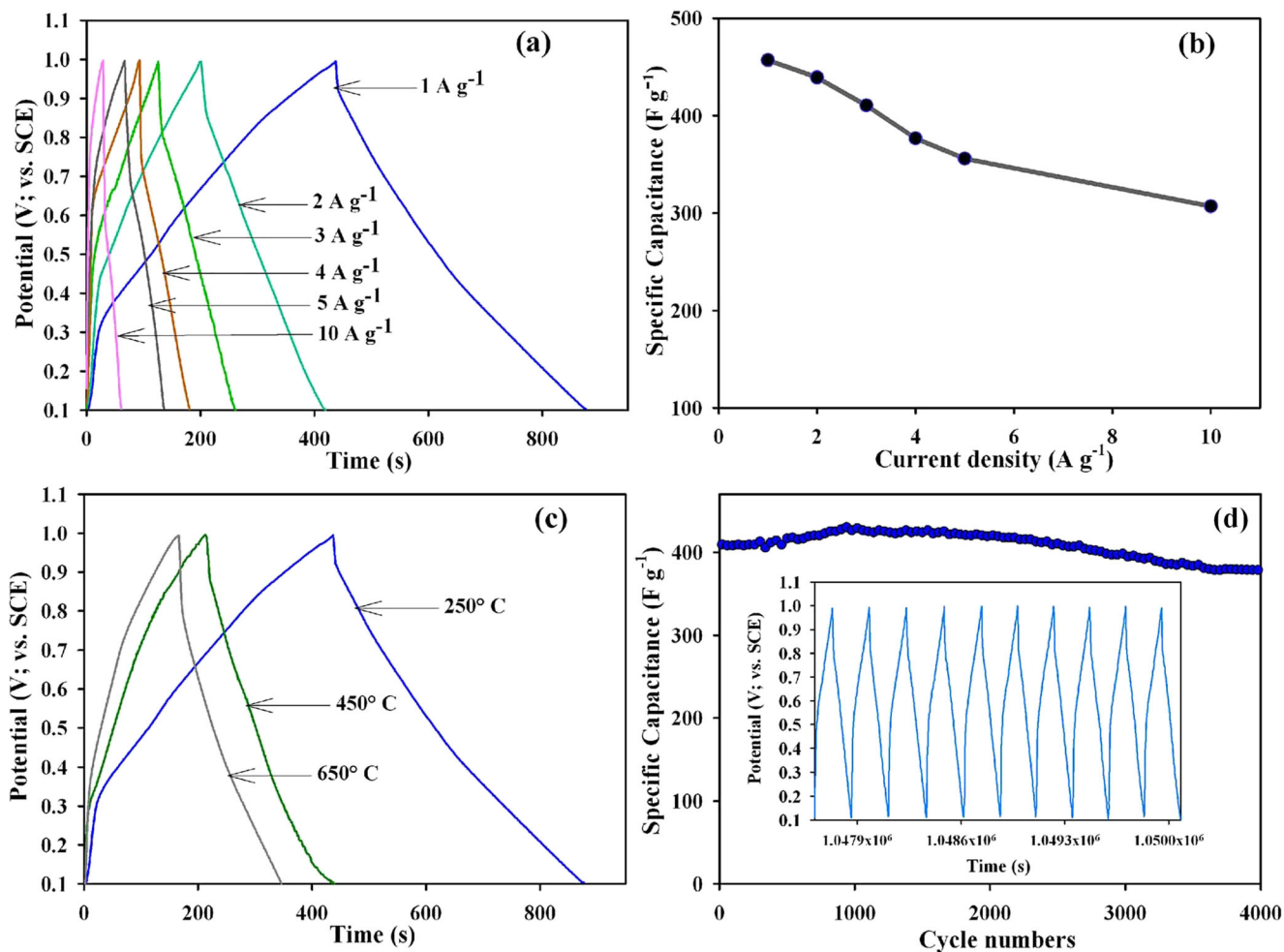
Fig. 8 **a** Charge-discharge curves of ZnMn₂O₄ nanosheet electrodes at different current densities. **b** The specific capacitance of the ZnMn₂O₄ nanosheet electrodes in 0.5 M Na₂SO₄ at different current densities. **c** Charge-discharge curves for ZnMn₂O₄ electrodes at 250, 450, and 650 °C measured at 1 A g⁻¹. **d** Cycling performance of the ZnMn₂O₄ nanosheet electrodes at the current density of 3 A g⁻¹. The inset shows the charge-discharge curves of the last 10 cycles of the ZnMn₂O₄

XPS measurement was used to characterize the elemental composition and oxidation state of the $ZnMn_2O_4$ nanosheets scratched from stainless steel, as shown in Fig. 5a, which exhibits photoelectron spectra for elements of Zn, Mn, and O. In Fig. 5b, the two major peaks at 642.1 and 653.7 eV can be attributed to Mn $2p_{3/2}$ and Mn $2p_{1/2}$ of $ZnMn_2O_4$ phase, respectively [39, 51]. Figure 5c represents Zn $2p$ spectra at binding energies of 1021.1 and 1044.2 eV, which can be imputed to Zn $2p_{3/2}$ and Zn $2p_{1/2}$, respectively, which is matching with previous reports [52, 53]. The spectrum of the O 1s spectra is depicted in Fig. 5d and fitted by two peaks at binding energies of 531.8 and 530.1 eV. More specifically, a fitted peak at a 530.1 eV is ascribed to lattice oxygen in $ZnMn_2O_4$ and the well-resolved peak at 531.8 eV attributed to oxygen in other components, such as H_2O and carbonate species adsorbed on the surface [52, 53]. Consequently, the XPS measurement confirmed that the ratio of Zn to Mn in the sample is very close to 1:2, which is in agreement with the EDX analysis.

To further investigation of the surface property of the $ZnMn_2O_4$, we evaluated the BET and nitrogen adsorption-desorption curves (Fig. 6a). The BET surface area of the $ZnMn_2O_4$ nanostructure at 250, 450, and 650 °C was calculated to be 51, 25, and 11 m^2 g^{-1}, respectively. These results exhibit that surface area of the $ZnMn_2O_4$ is decreased when calcination temperatures are raised. According to the

corresponding BJH plots (Fig. 6b) recorded from the nitrogen isotherms, the average pore size of $ZnMn_2O_4$ at 250 °C was obtained to be 63.2 nm. The good BET specific surface area and homogeneous pore distributions could effectively enhance the electrochemical reaction area and allow better penetration of the electrolyte that can result in a specific material for supercapacitor applications.

Electrochemical characterization

To investigate the applications of the nanostructures as supercapacitor, we fabricated electrodes in a three-electrode configuration. The Na_2SO_4 aqueous solution (0.5 M), platinum electrode, and saturated calomel electrode (SCE) were employed as electrolyte, counterelectrode, and reference electrode, respectively. The working electrode was prepared by mixing 80 wt% active material ($ZnMn_2O_4$), 15 wt% acetylene black, and 5 wt% polyvinylidene fluoride (PVDF) in N-methyl-2-pyrrolidone (NMP). The CV of $ZnMn_2O_4$ nanosheet electrodes (prepared at 250 °C) were obtained in 0.5 M Na_2SO_4 aqueous electrolyte in a potential window from 0.1 to 1 V at various scan rates (Fig. 7a). According to the CV curves, no distinction redox peaks were observed. The shape of CV curve deviates from the ideal rectangle that shows that prepared electrodes have a faradic pseudocapacitive nature. As the scan rate increases, the shape of the curve leads to

Fig. 9 **a** Nyquist impedance plots for devices with $ZnMn_2O_4$ electrodes at 250, 450, and 650 °C in 0.5 M Na_2SO_4, inset showing the high-frequency, low-impedance region. **b** Equivalent circuit model for the same devices mentioned in **a**
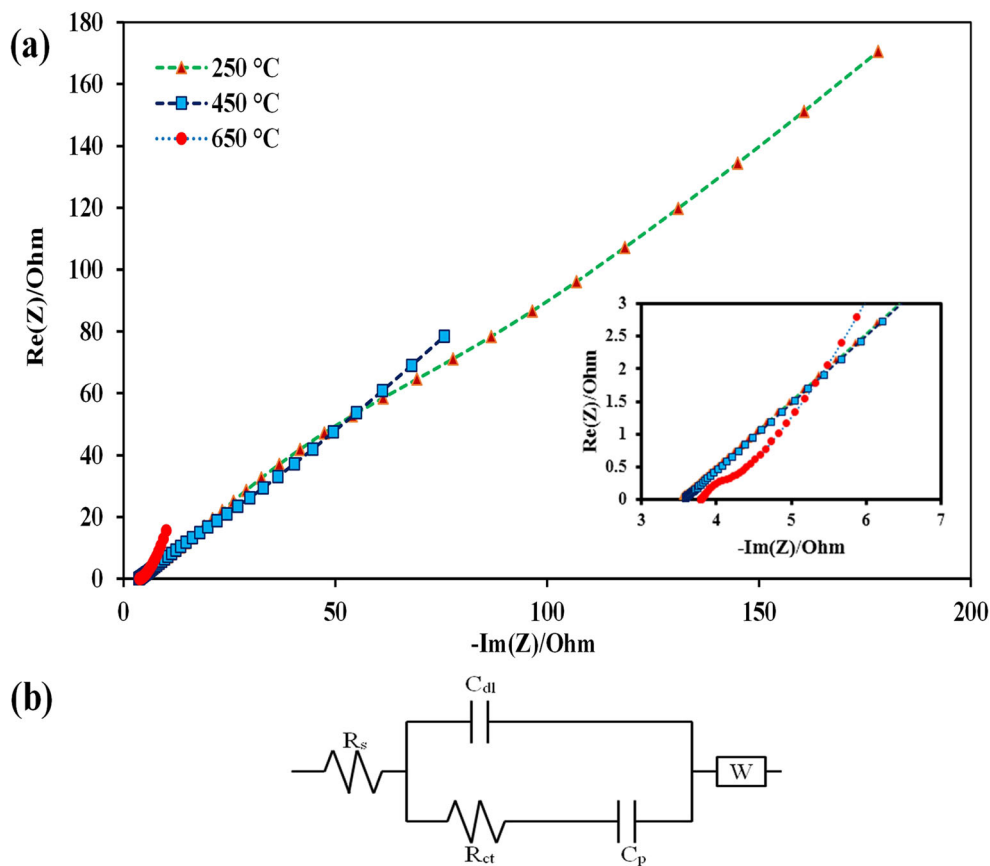
Table 1 The components of the equivalent circuit fitted for the impedance spectra of devices with ZnMn$_2$O$_4$ 250 °C, ZnMn$_2$O$_4$ 450 °C, and ZnMn$_2$O$_4$ 650 °C in 0.5 M Na$_2$SO$_4$

Sample	R_s (Ω cm^2)	R_{ct} (Ω cm^2)	W_s (Ω cm^2)	C_{dl} (F cm^{-2})	C_p (F cm^{-2})
ZnMn$_2$O$_4$ 250 °C	3.85	18.5	125.5	0.058	0.14
ZnMn$_2$O$_4$ 450 °C	3.56	2.95	55.6	0.034	0.16
ZnMn$_2$O$_4$ 650 °C	3.79	0.66	4.76	0.006	0.23

non-ideal form because of overpotentials [54]. The specific capacitance decreases with increasing in scan rate values. In general, at higher potential scan rates, charge transfer is found to be low and limit the diffusion rate of electrolyte into the electrode materials. These results can be explained as a results of limiting in ion access to active material and/or decreasing in interaction between the electrolyte ions and electrode [55, 56].

Figure 7b compares the CV behaviors of the ZnMn$_2$O$_4$ samples prepared at the different temperatures at sweep rate of 1 mV s^{-1}. The area of the CV curve for the ZnMn$_2$O$_4$ at 250 °C is large, whereas the CV area has decreased significantly at 450 °C and almost null at 650 °C, indicating the fading of charge-storage activity for crystalline ZnMn$_2$O$_4$.

To further evaluate electrochemical performances of the ZnMn$_2$O$_4$ synthesized at 250 °C electrode, galvanostatic charge-discharge tests were performed at the various current densities in an electrochemical window of 0.1 to 1 V (Fig. 8a). Here, appearing a linear slope and triangular symmetry is indicating the good electrochemical performance. The obtained C_s values were improved at lower current densities while it decreased with increasing in the current density. The specific capacitance of the ZnMn$_2$O$_4$ nanosheet electrodes calculated from each discharge curve is about 456.8, 439.2, 410.6, 376.8, 355.9, and 306.9 F g^{-1} at 1, 2, 3, 4, 5, and 10 A g^{-1}, respectively, as shown in Fig. 7b. It is worthy of noting that the ZnMn$_2$O$_4$ nanosheet electrode show a higher specific capacitance compared to the ZnMn$_2$O$_4$-based electrodes reported previously [41, 42]. Furthermore, from Fig. 8b, it can be seen that the capacitance of the ZnMn$_2$O$_4$ nanosheet electrode is slowly degraded with increase of the current densities from 1 to 10 A g^{-1}, and the retention of the specific capacitance is above 67.2%. The results illustrated that the ZnMn$_2$O$_4$ nanosheet electrode has good rate capability and great potential for applications in electrochemical capacitors.

Galvanostatic measurements (Fig. 8c) yield capacitances of 456.8, 229.9, and 180.0 F g^{-1} measured at constant current density of 1 A g^{-1} for supercapacitors prepared with

ZnMn$_2$O$_4$ 250, 450, and 650 °C, respectively. Further confirming observations were also obtained from the CV measurements in Fig. 7b. Two main reasons can be presented for specific capacitance decreases as calcining temperature increased. (1) Degree of crystallinity: although the high crystallinity in ZnMn$_2$O$_4$ can give rise to higher conductivity, the protonation (or deprotonation) reaction will be limited. Consequently, there should be a trade-off between electrical conductivity in the solid phase and ionic transport in the pore. (2) Specific surface area: normally, increases in the surface area of ZnMn$_2$O$_4$ imply more faradaic active sites and thereby higher pseudocapacitance. Therefore, the ZnMn$_2$O$_4$ exhibits superior performance at 250 °C than ZnMn$_2$O$_4$ at 450 and 650 °C which is because of optimum crystallinity and high specific surface area.

Figure 8d shows the cycling stability of the ZnMn$_2$O$_4$ nanosheet electrode at 250 °C by conducting charge/discharge tests at a current density of 3 A g^{-1} for 4000 cycles. The specific capacitance of the ZnMn$_2$O$_4$ nanosheet electrode maintains 92.5% of its initial value, indicating a good stability. The charge-discharge curves of the final 10 cycles are shown in inset of Fig. 9, showing almost the same symmetric shape. These results confirmed that, which implies that the ZnMn$_2$O$_4$ nanosheet electrode does not undergo significant structural change during the charge/discharge processes.

In order to understand the capacitive and resistance components associated with the ZnMn$_2$O$_4$ electrodes, electrochemical impedance spectroscopy studies were performed. Figure 9a shows the Nyquist spectra in the frequency range of 100 kHz to 10 mHz obtained at equilibrium open circuit potential (5 mV) at the different temperatures from 250 to 650 °C. An equivalent circuit simulating ZnMn$_2$O$_4$ electrodes with various calcining temperatures in 0.5 M Na$_2$SO$_4$ electrolyte would involve the following circuit elements: the electrolyte resistance (R_s), the double-layer capacitance (C_{dl}), the pseudocapacitance (C_p), the charge transfer resistance (R_{ct}), and the Warburg impedance due to distributed resistance

Table 2 Summary of ZnMn$_2$O$_4$-based supercapacitors with their key performance characteristics

Method of synthesis	Morphology	C_s (F g^{-1})	Electrolyte	Stability	Ref.
Urea combustion	Spherical	160	2 M KOH	0% loss after 500 cycles	[37]
Hydrothermal	Microsphere	155	2 M KOH	–	[38]
sucrose-assisted combustion	Hierarchical porous	411.75	6 M KOH	11.7% loss after 4000 cycles	[51]
ELD	Nanosheet	456.8	0.5 M Na$_2$SO$_4$	7.5% loss after 4000 cycles	This work

within the pores of $ZnMn_2O_4$ (W_s). The obtained values of these parameters in temperatures of 250, 450, and 650 °C are shown in Table 1.

The combination of the circuit elements proposed is shown in Fig. 9b. The electrolyte resistance was found to be small (3.56–3.85 Ω) and showed little variation for all devices. Here, the results showed that the charge R_{ct} decreases as the calcining temperature increases from 250 to 650 °C, indicating that the nanostructure of $ZnMn_2O_4$ synthesized at 650 °C with less hierarchical porosities is more accessible to the electrolyte ions as compared to $ZnMn_2O_4$ 250 and 450 °C. The same trend was observed for W_s, further confirming that $ZnMn_2O_4$ 650 has a less porous structure.

It is worth noting that $ZnMn_2O_4$ in 250 °C and $ZnMn_2O_4$ 450 °C have similar C_{dl}, which is mainly governed by the nanosheet and nanoflake morphologies of both obtained $ZnMn_2O_4$ which provide the electroactive surfaces needed for the charge transfer reaction and cation diffusion. On the other hand, $ZnMn_2O_4$ 650 has the lowest C_{dl} as compared to $ZnMn_2O_4$ 250 and 450 due to the its crystallinity structure, but the highest C_p because of its high crystallinity as revealed in SEM and XRD previously. According to the experiments, as the calcining temperature was increased from 250 to 650 °C, the obtained values for C_p are raised that could be expected due to the complete phase transformation into crystalline $ZnMn_2O_4$, and therefore, facile sites for the faradaic redox reaction would be more available. It should be considered that the obtained values for C_p in 250 °C are comparable with that ones in higher temperatures.

Finally, a comparison of the this work with previously reported methods for the application of $ZnMn_2O_4$ as electrode material in supercapacitor was presented (Table 2). Results showed that the $ZnMn_2O_4$ nanosheet synthesized with ELD method has a higher specific capacitanc and better stability than previous reports [41, 42, 57].

Conclusion

In summary, we have developed a facile and cost-effective method for preparing spinel $ZnMn_2O_4$ and the obtained samples were applied as electrodes of supercapacitor. The calcining temperature for the ELD of $ZnMn_2O_4$ has been optimized, and a temperature of 250 °C is found in best results. The selection of 250 °C as optimized calcining temperature was a result of experiment parameters including percent crystallization, morphology, surface area, and homogeneous pore distribution. SEM images showed that the calcining step has a shape-determining effect on the morphology of the sample. The spinel prepared at 250 °C consisting of nanosheets with long-range interconnectivity which creates electrochemical accessibility of ion electrolyte and a high diffusion rate through the bulk is obtained. The $ZnMn_2O_4$ nanosheet

electrode exhibits a specific capacitance of 456.8 F g^{-1} at a current density of 1 A g^{-1} and keeps the capacitance retention about 67.2% at 10 A g^{-1}. Furthermore, the retention of capacitance is 92.5% after 4000 cycles at current density of 3 A g^{-1} and the electrode shows excellent stability. The $ZnMn_2O_4$ nanostructure was synthesized by ELD method with remarkably enhanced capacitive behaviors, and it can be extendable to other spinel-type oxide and transition metal oxide systems.

References

1. Liu C, Li F, Ma LP, Cheng HM (2010) Advanced materials for energy storage. Adv Mater 22:28–62. https://doi.org/10.1002/adma.200903328
2. Simon P, Gogotsi Y (2008) Materials for electrochemical capacitors. Nat Mater 7:845–854. https://doi.org/10.1038/nmat2297
3. Winter M, Brodd RJ (2004) What are batteries, fuel cells, and supercapacitors? Chem Rev 104:4245–4270. https://doi.org/10.1021/cr020730k
4. Miller JR, Simon P (2008) Electrochemical capacitors for energy management. Sci Mag 321:651–652. https://doi.org/10.1126/science.1158736
5. Simon P, Gogotsi Y, Dunn B (2014) Where do batteries end and supercapacitors begin? Science 343:1210–1211. https://doi.org/10.1126/science.1249625
6. Yan J, Wang Q, Wei T, Fan Z (2014) Recent advances in design and fabrication of electrochemical supercapacitors with high energy densities. Adv Energy Mater 4:1300816–1130059. https://doi.org/10.1002/aenm.201300816
7. Chen D, Tang L, Li J (2010) Graphene-based materials in electrochemistry. Chem Soc Rev 39:3157–3180. https://doi.org/10.1039/B923596E
8. Itagaki M, Suzuki S, Shitanda I, Watanabe K, Nakazawa H (2007) Impedance analysis on electric double layer capacitor with transmission line model. J Power Sources 164:415–424. https://doi.org/10.1016/j.jpowsour.2006.09.077
9. Wang G, Zhang L, Zhang J (2012) A review of electrode materials for electrochemical supercapacitors. Chem Soc Rev 41:797–828. https://doi.org/10.1039/C1CS15060J
10. He S, Hu C, Hou H, Chen W (2014) Ultrathin MnO_2 nanosheets supported on cellulose based carbon papers for high-power supercapacitors. J Power Sources 246:754–761. https://doi.org/10.1016/j.jpowsour.2013.08.038
11. Chang J, Jin M, Yao F, Kim TH, Le VT, Yue H, Gunes F, Li B, Ghosh A, Xie S (2013) Asymmetric supercapacitors based on graphene/MnO_2 nanospheres and graphene/MoO_3 nanosheets with high energy density. Adv Funct Mater 23:5074–5083. https://doi.org/10.1002/adfm201301851
12. Yuan C, Li J, Hou L, Yang L, Shen L, Zhang X (2012) Facile growth of hexagonal NiO nanoplatelet arrays assembled by mesoporous nanosheets on Ni foam towards high-performance electrochemical capacitors. Electrochim Acta 78:532–538. https://doi.org/10.1016/j.electacta.2012.06.044
13. Purushothaman KK, Manohara Babu I, Sethuraman B, Muralidharan G (2013) Nanosheet-assembled NiO microstructures for high-performance supercapacitors. ACS Appl Mater Interfaces 5:10767–10773. https://doi.org/10.1021/am402869p

14. Yuan C, Yang L, Hou L, Shen L, Zhang X, Lou XWD (2012) Growth of ultrathin mesoporous Co_3O_4 nanosheet arrays on Ni foam for high-performance electrochemical capacitors. Energy Environ Sci 5:7883–7887. https://doi.org/10.1039/C2EE21745G

15. Du W, Liu R, Jiang Y, Lu Q, Fan Y, Gao F (2013) Facile synthesis of hollow Co_3O_4 boxes for high capacity supercapacitor. J Power Sources 227:101–105. https://doi.org/10.1016/j.jpowsour.2012.11.009

16. Lu Y, Yan H, Qiu K, Cheng J, Wang W, Liu X, Tang C, Kim J-K, Luo Y (2015) Hierarchical porous CuO nanostructures with tunable properties for high performance supercapacitors. RSC Adv 5:10773–10781. https://doi.org/10.1039/C4RA16924G

17. Ye J, Li Z, Dai Z, Zhang Z, Guo M, Wang X (2016) Facile synthesis of hierarchical CuO nanoflower for supercapacitor electrodes. J Electron Mater 45:4237–4245. https://doi.org/10.1007/s11664-016-4587-1

18. Jiang J, Li Y, Liu J, Huang X, Yuan C, Lou XWD (2012) Recent advances in metal oxide-based electrode architecture design for electrochemical energy storage. Adv Mater 24:5166–5180. https://doi.org/10.1002/adma.201202146

19. Jiang H, Ma J, Li C (2012) Hierarchical porous $NiCo_2O_4$ nanowires for high-rate supercapacitors. Chem Commun 48:4465–4467. https://doi.org/10.1039/C2CC31418E

20. Zhang G, Lou XWD (2013) General solution growth of mesoporous $NiCo_2O_4$ nanosheets on various conductive substrates as high-performance electrodes for supercapacitors. Adv Mater 25:976–979. https://doi.org/10.1002/adma.201204128

21. Sharma Y, Sharma N, Rao GS, Chowdari B (2008) Studies on spinel cobaltites, $FeCo_2O_4$ and $MgCo_2O_4$ as anodes for Li-ion batteries. Solid State Ionics 179:587–597. https://doi.org/10.1016/j.ssi.2008.04.007

22. Zhang G, Xia BY, Xiao C, Yu L, Wang X, Xie Y, Lou XWD (2013) General formation of complex tubular nanostructures of metal oxides for the oxygen reduction reaction and lithium-ion batteries. Angew Chem Int Ed 125:8805–8809. https://doi.org/10.1002/ange.201304355

23. Sharma Y, Sharma N, Subba Rao G, Chowdari B (2007) Nanophase $ZnCo_2O_4$ as a high performance anode material for Li-ion batteries. Adv Funct Mater 17:2855–2861. https://doi.org/10.1002/adfm.200600997

24. Karthikeyan K, Kalpana D, Renganathan N (2009) Synthesis and characterization of $ZnCo_2O_4$ nanomaterial for symmetric supercapacitor applications. Ionics 15:107–110. https://doi.org/10.1007/s11581-008-0227-y

25. Heydari H, Gholivand MB (2017) Novel synthesis and characterization of $ZnCo_2O_4$ nanoflakes grown on nickel foam as efficient electrode materials for electrochemical supercapacitors. Ionics 23:1489–1498. https://doi.org/10.1007/s11581-016-1959-8

26. Wang Z, Zhang X, Li Y, Liu Z, Hao Z (2013) Synthesis of graphene–$NiFe_2O_4$ nanocomposites and their electrochemical capacitive behavior. J Mater Chem A 1:6393–6399

27. Xiao J, Yang S (2011) Sequential crystallization of sea urchin-like bimetallic (Ni, Co) carbonate hydroxide and its morphology conserved conversion to porous $NiCo_2O_4$ spinel for pseudocapacitors. RSC Adv 1:588–595. https://doi.org/10.1039/C1RA00342A

28. Zhang X-D, Wu Z-S, Zang J, Li D, Zhang Z-D (2007) Hydrothermal synthesis and characterization of nanocrystalline Zn–Mn spinel. J Phys Chem Solids 68:1583–1590. https://doi.org/10.1016/j.jpcs.2007.03.044

29. He W, Wang C, Li H, Deng X, Xu X, Zhai T (2017) Ultrathin and porous $Ni_3S_2/CoNi_2S_4$ 3D-network structure for superhigh energy density asymmetric supercapacitors. Adv Energy Mater 7:1700983–1700994. https://doi.org/10.1002/aenm.201700983

30. Yu X, Lu B, Xu Z (2014) Super long-life supercapacitors based on the construction of nanohoneycomb-like strongly coupled $CoMoO_4$–3D graphene hybrid electrodes. Adv Mater 26:1044–1051. https://doi.org/10.1002/aenm.201700983

31. Wang C, Guo K, He W, Deng X, Hou P, Zhuge F, Xu X, Zhai T (2017) Hierarchical $CuCo2O4@$ nickel-cobalt hydroxides core/shell nanoarchitectures for high-performance hybrid supercapacitors. Sci Bull 62:1122–1131. https://doi.org/10.1016/j.scib.2017.08.014

32. Sun P, Wang C, He W, Hou P, Xu X (2017) One-step synthesis of 3D network-like $Ni_x Co_{1-x} MoO_4$ porous Nanosheets for high performance battery-type hybrid supercapacitors. ACS Sustain Chem Eng 5:10139–10147. https://doi.org/10.1021/acssuschemeng.7b02143

33. Liu Y, Wang Y, Xu X, Sun P, Chen T (2014) Facile one-step room-temperature synthesis of Mn-based spinel nanoparticles for electro-catalytic oxygen reduction. RSC Adv 4:4727–4731. https://doi.org/10.1039/C3RA47065B

34. Zhang G, Yu L, Wu HB, Hoster HE, Lou XWD (2012) Formation of $ZnMn_2O_4$ ball-in-ball hollow microspheres as a high-performance anode for lithium-ion batteries. Adv Mater 24:4609–4613. https://doi.org/10.1002/adma.201201779

35. Bhandage G, Keer H (1978) Magnetic properties of the $ZnMn_2O_4$-$NiMn_2O_4$ system. J Phys C Solid State Phys 11:219–221. https://doi.org/10.1088/0022-3719/11/6/008

36. Teh PF, Sharma Y, Ko YW, Pramana SS, Srinivasan M (2013) Tuning the morphology of $ZnMn_2O_4$ lithium ion battery anodes by electrospinning and its effect on electrochemical performance. RSC Adv 3:2812–2821. https://doi.org/10.1039/C2RA22943A

37. Wang N, Ma X, Xu H, Chen L, Yue J, Niu F, Yang J, Qian Y (2014) Porous $ZnMn_2O_4$ microspheres as a promising anode material for advanced lithium-ion batteries. Nano Energy 6:193–199. https://doi.org/10.1016/j.nanoen.2014.04.001

38. Jin R, Wen Q, Yang L, Li G (2014) $ZnMn_2O_4$ mesocrystals for lithium-ion batteries with high rate capacity and cycle stability. Mater Lett 135:55–58. https://doi.org/10.1016/j.matlet.2014.07.132

39. Kim S-W, Lee H-W, Muralidharan P, Seo D-H, Yoon W-S, Kim DK, Kang K (2011) Electrochemical performance and ex situ analysis of $ZnMn_2O_4$ nanowires as anode materials for lithium rechargeable batteries. Nano Res 4:505–510. https://doi.org/10.1007/s12274-011-0106-0

40. Yang Y, Zhao Y, Xiao L, Zhang L (2008) Nanocrystalline $ZnMn_2O_4$ as a novel lithium-storage material. Electrochem Commun 10:1117–1120. https://doi.org/10.1016/j.elecom.2008.05.026

41. Sahoo A, Sharma Y (2015) Synthesis and characterization of nanostructured ternary zinc manganese oxide as novel supercapacitor material. Mater Chem Phys 149:721–727. https://doi.org/10.1016/j.matchemphys.2014.11.032

42. Guo N, Wei X, Deng X, Xu X (2015) Synthesis and property of spinel porous $ZnMn_2O_4$ microspheres. Appl Surf Sci 356:1127–1134. https://doi.org/10.1016/j.apsusc.2015.08.185

43. Zhitomirsky I (2002) Cathodic electrodeposition of ceramic and organoceramic materials. Fundamental aspects. Adv Colloid Interf 97:279–317. https://doi.org/10.1016/S0001-8686(01)00068-9

44. Gal-Or L, Silberman I, Chaim R (1991) Electrolytic ZrO_2 coatings I. Electrochemical aspects. J Electrochem Soc 138:1939–1942. https://doi.org/10.1149/1.2085904

45. Therese GHA, Kamath PV (2000) Electrochemical synthesis of metal oxides and hydroxides. Chem Mater 12:1195–1204. https://doi.org/10.1021/cm990447a

46. Chen Y, Xie K, Pan Y, Zheng C (2010) Effect of calcination temperature on the electrochemical performance of nanocrystalline $LiMn_2O_4$ prepared by a modified resorcinol–formaldehyde route. Solid State Ionics 181:1445–1450. https://doi.org/10.1016/j.ssi.2010.08.011

47. Oh SW, Bang HJ, Bae YC, Sun Y-K (2007) Effect of calcination temperature on morphology, crystallinity and electrochemical properties of nano-crystalline metal oxides (Co_3O_4, CuO, and NiO) prepared via ultrasonic spray pyrolysis. J Power Sources 173: 502–509. https://doi.org/10.1016/j.jpowsour.2007.04.087

48. Liu Y, Zhang X (2009) Effect of calcination temperature on the morphology and electrochemical properties of Co_3O_4 for lithium-ion battery. Electrochim Acta 54:4180–4185. https://doi.org/10.1016/j.electacta.2009.02.060

49. Moazami HR, Davarani SSH, Yousefi T, Keshtkar AR (2015) Synthesis of manganese dioxide nanosheets and charge storage evaluation. Mater Sci Semicond Process 30:682–687. https://doi.org/10.1016/j.mssp.2014.09.002

50. Selim M, Deraz N, Elshafey O, El-Asmy A (2010) Synthesis, characterization and physicochemical properties of nanosized Zn/Mn oxides system. Alloys Compd 506:541–547. https://doi.org/10.1016/j.jallcom.2010.04.180

51. Deng Y, Tang S, Zhang Q, Shi Z, Zhang L, Zhan S, Chen G (2011) Controllable synthesis of spinel nano-$ZnMn_2O_4$ via a single source precursor route and its high capacity retention as anode material for lithium ion batteries. J Mater Chem A 21:11987–11995. https://doi.org/10.1039/C1JM11575H

52. Kim JG, Lee SH, Kim Y, Kim WB (2013) Fabrication of freestanding $ZnMn_2O_4$ mesoscale tubular arrays for lithium-ion anodes with highly reversible lithium storage properties. ACS Appl Mater Interfaces 5:11321–11328. https://doi.org/10.1021/am403546s

53. Zhang P, Li X, Zhao Q, Liu S (2011) Synthesis and optical property of one-dimensional spinel $ZnMn_2O_4$ nanorods. Nanoscale Res Lett 6:1–8. https://doi.org/10.1186/1556-276X-6-323

54. He Y, Chen W, Li X, Zhang Z, Fu J, Zhao C, Xie E (2012) Freestanding three-dimensional graphene/MnO_2 composite networks as ultralight and flexible supercapacitor electrodes. ACS Nano 7:174–182. https://doi.org/10.1021/nn304833s

55. Dai K, Liang C, Dai J, Lu L, Zhu G, Liu Z, Liu Q, Zhang Y (2014) High-yield synthesis of carbon nanotube–porous nickel oxide nanosheet hybrid and its electrochemical capacitance performance. Mater Chem Phys 143:1344–1351. https://doi.org/10.1016/j.matchemphys.2013.11.045

56. Hu L, Chen W, Xie X, Liu N, Yang Y, Wu H, Yao Y, Pasta M, Alshareef HN, Cui Y (2011) Symmetrical MnO_2–carbon nanotube–textile nanostructures for wearable pseudocapacitors with high mass loading. ACS Nano 5:8904–8913. https://doi.org/10.1021/nn203085j

57. Huang T, Zhao C, Qiu Z, Luo J, Hu Z (2017) Hierarchical porous $ZnMn_2O_4$ synthesized by the sucrose-assisted combustion method for high-rate supercapacitors. Ionics 23:139–146. https://doi.org/10.1007/s11581-016-1817-8